Chinese Journal of Chemical Engineering 90 (2026) 293–307

Contents lists available at ScienceDirect

Chinese Journal of Chemical Engineering

journal homepage: www.elsevier.com/locate/CJChE

Full Length Article

Multiscale synergistic enhancement mechanism of solid–liquid mixing in multi-shaft stirred reactors under variable-speed operation

Tong Meng [1, 2, 3], Yu Wang [1, 3], Yijuan Tian [1, 3], Shuang Qin [1, 3], Yuyan Lin [1, 3], Peiqiao Liu [1], Yundong Wang [4], Zuohua Liu [1, 3, *]

[1] School of Chemistry and Chemical Engineering, Chongqing University, Chongqing 400044, China
[2] Department of Industrial Chemistry "Toso Montanari", University of Bologna, Bologna 40131, Italy
[3] State Key Laboratory of Coal Mine Disaster Dynamics and Control, Chongqing 400044, China
[4] Department of Chemical Engineering, Tsinghua University, Beijing 100084, China

ARTICLE INFO

Article history:
Received 29 July 2025
Received in revised form
25 September 2025
Accepted 25 September 2025
Available online 11 November 2025

Keywords:
Multi-shaft stirred reactors
Two-phase flow
Mixing
Computational fluid dynamics
Multiscale
Dynamic mode decomposition

ABSTRACT

Research on the solid–liquid mixing process and its enhancement mechanisms in multi-shaft stirred reactors still face challenges that limit its industrial applications. This work employs the RNG k–ε model combined with the EE-KTGF model to numerically simulate the solid–liquid mixing process within a multi-shaft stirred reactor, yielding satisfactory results when compared to experimental data. Comparative analysis of the solid–liquid mixing performance under four different operational conditions reveals that applying variable speed conditions to the bottom impeller results in a smaller solid concentration gradient, reduced particle settling rates, and an improvement in solid homogeneity by 2.74% to 3.22% compared to other operational conditions. This operational condition enables more effective suspension and uniform distribution of solid particles throughout the reactor, thereby enhancing overall mixing efficiency. Flow field analysis under different operational conditions indicates that applying variable speed to the bottom impeller significantly improves flow field stability, reduces axial back-mixing, and optimizes the axial distribution of solid particles. Further dynamic mode decomposition of the flow field and time series analysis of modal coefficients elucidate a multi-scale synergistic nesting chaos-enhanced mechanism characterized by "macroscopic stability, mesoscopic matching, and microscopic resonance". This work provides a theoretical foundation for the design and operational optimization of multi-shaft stirred reactors.

1. Introduction

The solid–liquid mixing process plays a critical role in several frontier fields, including renewable resource conversion, energy-efficient separation, material synthesis, and biomanufacturing [1,2]. As the demand for resource utilization efficiency and process stability continues to rise, the solid–liquid mixing process faces significant challenges related to supply and demand imbalance. This has driven the development of solid–liquid reactors towards larger scales and increased automation [3]. Among various solid–liquid mixing technologies, mechanical stirring is by far the most common and widely applied, covering more than 95% of industrial production [4]. Despite substantial research aimed at enhancing the performance of mixing reactors—through the optimization of operational conditions [5], impeller types [6–8] and baffle configurations [9]—most improvements have been focused on single-shaft or coaxial mixing reactors, with limited exploration of more complex reactor systems [10,11]. Thus, there is a growing need for further investigation into innovative technologies for the solid–liquid mixing process, particularly in the design of multi-shaft, multi-impeller, or intelligent reactors, which holds significant theoretical value and application potential [12,13].

In particular, for large-scale stirring reactors, single-shaft stirring reactors exhibit notable shortcomings when addressing challenges related to scale expansion and the demand for automation [14]. For instance, the increased size of reactor components leads to significant challenges in machining, and torque overload is a common issue during operation. Additionally, in the context of

* Corresponding author.
E-mail address: liuzuohua@cqu.edu.cn (Z. Liu).

https://doi.org/10.1016/j.cjche.2025.09.024

automation, the limited feedback targets lead to weaker adaptive control capabilities. In recent years, researchers have turned their attention to multi-shaft stirring reactors, which have been demonstrated to offer unique advantages in energy optimization, improved mixing performance, and intelligent control [15–18]. However, research related to multi-shaft stirring reactors, such as spindle positioning and group control strategies, remains largely focused on single-phase or simple reaction systems [16]. Systematic studies on multi-shaft stirring reactors for solid–liquid mixing processes are still lacking. Therefore, this work aims to expand and deepen prior research, exploring the applications and performance of multi-shaft stirring reactors across different systems, thereby providing theoretical support and technological insights for the optimization and innovation of solid–liquid mixing processes.

In this work, a particle volume fraction of 10% was selected, which is significantly higher than the 5% typically defined as the threshold for high-concentration in mechanical stirring reactors in most previous studies, classifying it as a high solid-content mixing system [19]. Under such high-solid conditions, the interaction between the liquid phase mixing process and the suspended particles is highly complex, posing considerable challenges for the application of traditional experimental techniques. High-concentration particles lead to a turbid flow field, making common optical measurement techniques, such as particle image velocimetry (PIV) and laser Doppler velocimetry (LDV), unsuitable for this scenario [20]. On the other hand, experimental tools like nuclear magnetic resonance (NMR) can offer high-precision measurements, but their high cost and stringent experimental requirements render them impractical for monitoring solid–liquid mixing processes in large-scale industrial applications [21]. In recent years, novel measurement techniques such as electrical resistance tomography (ERT) and electrical capacitance tomography (ECT) have attracted increasing attention for solid–liquid mixing processes. However, due to their relatively low resolution, these methods struggle to effectively characterize more complex solid–liquid mixing processes [22]. Another promising technology, ultrasound imaging velocimetry (UIV), has gained considerable interest in both academia and industry in recent years. Although primarily used in the medical field, there is still significant potential for its application in industrial settings, particularly in complex multiphase flows, which remains to be fully explored [23]. Given the limitations of the aforementioned techniques, computational fluid dynamics (CFD) remains a crucial tool for the quantitative and qualitative analysis of complex multiphase mixing processes [24]. CFD provides a more accurate approach for understanding the flow behaviors and interactions in high solid content mixing systems.

The suspension mechanism of solid particles in the solid–liquid mixing process of stirred reactors is a critical area of research. In the context of solid–liquid mixing studies based on CFD, the description of interactions between particles and between particles and the fluid is fundamental [25]. Currently, two primary methods are widely applied in the simulation of solid–liquid suspension and mixing processes: the Euler–Lagrange (EL) method and the Euler–Euler (EE) method [26,27]. In the EL method, each particle is treated as an independent entity, and its motion is described by solving the equations of motion for each individual particle. As a result, this method is suitable for cases involving a small number of particles and is computationally expensive, making it less applicable to industrial-scale solid–liquid mixing processes in stirred reactors [28,29]. In contrast, the EE method treats the particle phase as a continuous fluid phase, assuming that particles and the fluid interact, and can permeate each other, with continuity and momentum equations solved separately for each phase under the same pressure conditions. This method is well-suited for dense systems and has been widely adopted by most researchers, leading to numerous significant findings [25,30,31]. For example, Gu *et al.* [6] used the standard k–ε turbulence model and the EE method to compare the solid–liquid mixing performance and power consumption of a self-similar impeller and a pitched-blade impeller at the same impeller speed. The results showed that, under constant power consumption, the self-similar impeller could enhance the suspension of solid particles, and the effect became more pronounced as the number of self-similar iterations increased. Kasat *et al.* [19], using the same turbulence model and EE method, simulated the solid–liquid mixing process in a single-shaft single-blade impeller stirred reactor and identified that the very low liquid velocity in the top transparent liquid layer was the main cause of delayed mixing. Hosseini *et al.* [32], employing the same method, investigated the effects of different impeller types (Lightnin A100, A200, and A310), impeller clearance ($T/6$–$T/2$, where T is the tank diameter), impeller speed (150–800 $\mathrm{r\cdot min^{-1}}$), particle size (100–900 μm), and particle density (1.4–6) on mixing performance. His results indicated that the A100 impeller was more efficient in terms of homogeneity compared to the A310 and A200 impellers, and for solid suspension systems, the optimal impeller clearance was $T/3$. Additionally, the study demonstrated that the physical properties of solid particles, such as particle size and density, significantly affect the homogeneity of the solid–liquid mixing process. However, traditional EE methods overlook the impact of particle–particle collisions, a crucial factor in dense solid–liquid suspensions. To address this, Gidaspow [33] introduced the kinetic theory of granular flow (KTGF) model, which considers the effects of particle collisions. The combination of the EE method and the KTGF model has been shown to provide reliable predictions of particle distribution and velocity in dense-phase solid–liquid stirred tanks, with validation of its effectiveness [11,31,34,35].

In the solid–liquid mixing process of stirred reactors, turbulence modeling is equally critical. Turbulence modeling typically involves three primary methods: direct numerical simulation (DNS), large eddy simulation (LES), and Reynolds-averaged Navier–Stokes (RANS) equations [36]. Among these, the RANS method is widely considered the most economical and practical choice for industrial-scale solid–liquid mixing reactors, due to its computational efficiency, a viewpoint broadly accepted within the academic community [35,37]. Within the RANS approach, the k–ε model is one of the most commonly used models. This model is further divided into the standard k–ε model, the RNG k–ε model, and the realizable k–ε model. Although there has been no consensus on the selection of a specific model across various studies, all three models have been shown to yield reasonably accurate results [34]. Recent research by Xu *et al.* [11] compared these three models with experimental measurements and found that the RNG model provides the best predictive accuracy. As a result, the combination of the RNG k–ε model with the EE-KTGF model has gradually become the mainstream approach in recent solid–liquid mixing studies [34,38–40]. Notably, the turbulent flow in multi-shaft stirred reactor exhibits pronounced spatiotemporal multiscale behavior and strong unsteadiness [14,17,41]. In solid–liquid mixing, bidirectional solid–fluid coupling further amplifies this complexity, complicating efforts to elucidate how flow structures form and interact. Data-driven reduced-order methods, such as dynamic mode decomposition (DMD), can extract coherent structures and dominant modes from high-dimensional flow data, reveal the key physics, and enable interpretable model reduction. Our prior work shows that DMD-based analysis can identify wave–vortex coupling in multi-shaft stirred flows and assess its impact on mixing [15]. The method

has also been applied to interrogate various mechanisms in stirred reactors, demonstrating strong applicability [17,42–45].

In this work, the RNG k–ε model combined with the EE-KTGF model was employed to numerically simulate the solid–liquid mixing process in a multi-shaft stirred reactor. The accuracy of the simulation results was validated through comparison with experimental data. Importantly, this work primarily applied variable rotational speed conditions to different shafts, conducting both qualitative and quantitative analyses of their solid–liquid mixing performance and flow field characteristics, ultimately determining the optimal operating conditions. The use of low-speed operating conditions facilitated a detailed investigation of fundamental flow phenomena in the solid–liquid mixing process. To further understand these phenomena, DMD was employed to analyze the transient flow field. This analysis provided deeper insights into the role of synergistic nesting mechanisms of multi-scale vortex structures in enhancing solid–liquid mixing performance. Overall, the findings from this work offer essential theoretical insights for optimizing operating conditions and implementing intelligent control in multi-shaft stirred reactors used for solid–liquid mixing processes.

2. Governing Equations and Mathematical Model

2.1. EE model

This work simulates the solid–liquid mixing within a multi-shaft stirred reactor using the EE model framework, where the motion of different phases is computed through the continuity and momentum equations.

Continuity equation is

$$\frac{\partial\left(\alpha_f\rho_f\right)}{\partial t}+\nabla\left(\alpha_f\rho_f\boldsymbol{v}_f\right)=0 \tag{1}$$

Momentum equation is

$$\frac{\partial}{\partial t}(\alpha_{\mathrm{L}}\rho_{\mathrm{L}}\boldsymbol{v}_{\mathrm{L}})+\nabla(\alpha_{\mathrm{L}}\rho_{\mathrm{L}}\boldsymbol{v}_{\mathrm{L}}\boldsymbol{v}_{\mathrm{L}})=-\alpha_{\mathrm{L}}\nabla P+\nabla\overline{\overline{\boldsymbol{\tau}}}_{\mathrm{L}}+\alpha_{\mathrm{L}}\rho_{\mathrm{L}}\boldsymbol{g}+\boldsymbol{F}_{\mathrm{DL}}+\boldsymbol{F}_{\mathrm{TL}} \tag{2}$$

$$\frac{\partial}{\partial t}(\alpha_{\mathrm{S}}\rho_{\mathrm{S}}\boldsymbol{v}_{\mathrm{S}})+\nabla(\alpha_{\mathrm{S}}\rho_{\mathrm{S}}\boldsymbol{v}_{\mathrm{S}}\boldsymbol{v}_{\mathrm{S}})=-\alpha_{\mathrm{S}}\nabla P+\nabla\overline{\overline{\boldsymbol{\tau}}}_{\mathrm{S}}+\alpha_{\mathrm{S}}\rho_{\mathrm{S}}\boldsymbol{g}-\nabla P_{\mathrm{S}}+\boldsymbol{F}_{\mathrm{DS}}+\boldsymbol{F}_{\mathrm{TS}} \tag{3}$$

where, α, ρ, and $\boldsymbol{v}$ represent the concentration, density, and velocity of the different phases, respectively. The subscript f denotes the phases, with S referring to the solid phase and L to the liquid phase. $\boldsymbol{g}$ represents gravitational acceleration, while $\boldsymbol{F}_{\mathrm{Df}}$ ($\boldsymbol{F}_{\mathrm{DS}}$ & $\boldsymbol{F}_{\mathrm{DL}}$) and $\boldsymbol{F}_{\mathrm{Tf}}$ ($\boldsymbol{F}_{\mathrm{TS}}$ & $\boldsymbol{F}_{\mathrm{TL}}$) correspond the drag forces and turbulent dispersion forces, respectively. P and P_{S} represent the pressure shared by all phases and the solid-phase pressure, respectively. The equations for the liquid stress tensor ($\overline{\overline{\boldsymbol{\tau}}}_{\mathrm{L}}$) and solid stress tensor ($\overline{\overline{\boldsymbol{\tau}}}_{\mathrm{S}}$) are as follows:

$$\overline{\overline{\boldsymbol{\tau}}}_{\mathrm{L}}=\alpha_{\mathrm{L}}\mu_{\mathrm{L}}\left[\nabla\boldsymbol{v}_{\mathrm{L}}+\nabla\boldsymbol{v}_{\mathrm{L}}{}^{\mathrm{T}}-\frac{2}{3}(\nabla\cdot\boldsymbol{v}_{\mathrm{L}})\boldsymbol{I}\right] \tag{4}$$

$$\overline{\overline{\boldsymbol{\tau}}}_{\mathrm{S}}=\alpha_{\mathrm{S}}\mu_{\mathrm{S}}\left(\nabla\boldsymbol{v}_{\mathrm{S}}+\nabla\boldsymbol{v}_{\mathrm{S}}{}^{\mathrm{T}}\right)+\alpha_{\mathrm{S}}\left(\lambda_{\mathrm{S}}-\frac{2}{3}\mu_{\mathrm{S}}\right)(\nabla\cdot\boldsymbol{v}_{\mathrm{S}})\boldsymbol{I} \tag{5}$$

where, μ_{L} denotes the liquid shear viscosity, μ_{S} represents the solid shear viscosity, and λ_{S} refers to the solid bulk viscosity.

The formulation of all the above equations must satisfy the following conditions:

$$\alpha_{\mathrm{L}}+\alpha_{\mathrm{S}}=1 \tag{6}$$

2.2. Interphase force model

The interactions between the solid and liquid phases include drag force, turbulent dispersion force, virtual mass force, lift force, and others. Among these, virtual mass force and lift force are often neglected by most researchers due to their minimal impact. Therefore, in this work, only drag force and turbulent dispersion force are considered [11,19,40]. In Fluent, several models are available for drag force and turbulent dissipation, providing users with multiple options [46]. Based on prior research and empirical experience [6,11,34], the Ding and Gidaspow [47] and Burns *et al.* [48] models have been selected for the formulation of drag and turbulent dispersion forces in this work.

The Gidaspow drag force model is constructed as follows:

$$\boldsymbol{F}_{\mathrm{DS}}=-\boldsymbol{F}_{\mathrm{DL}}=K_{\mathrm{SL}}(\boldsymbol{v}_{\mathrm{S}}-\boldsymbol{v}_{\mathrm{L}}) \tag{7}$$

where, the definition of the interphase exchange coefficient K_{SL} is as follows:

$$K_{\mathrm{SL}}=150\frac{\alpha_{\mathrm{S}}(1-\alpha_{\mathrm{L}})\mu_{\mathrm{L}}}{\alpha_{\mathrm{L}}d_{\mathrm{S}}^2}+1.75\frac{\rho_{\mathrm{L}}\alpha_{\mathrm{S}}|\boldsymbol{v}_{\mathrm{S}}-\boldsymbol{v}_{\mathrm{L}}|}{d_{\mathrm{S}}}\quad(\alpha_{\mathrm{L}}\le 0.8) \tag{8}$$

$$K_{\mathrm{SL}}=\frac{3}{4}C_{\mathrm{D}}\frac{\alpha_{\mathrm{S}}\alpha_{\mathrm{L}}\rho_{\mathrm{L}}|\boldsymbol{v}_{\mathrm{S}}-\boldsymbol{v}_{\mathrm{L}}|}{d_{\mathrm{S}}}\alpha_{\mathrm{L}}{}^{-2.65}\quad(\alpha_{\mathrm{L}}>0.8) \tag{9}$$

where, the definition of the drag coefficient C_{D} is as follows:

$$C_{\mathrm{D}}=\frac{24}{\alpha_{\mathrm{L}}Re_{\mathrm{S}}}\left[1+0.15(\alpha_{\mathrm{L}}Re_{\mathrm{S}})^{0.687}\right] \tag{10}$$

$$Re_{\mathrm{S}}=\frac{\rho_{\mathrm{L}}d_{\mathrm{S}}|\boldsymbol{v}_{\mathrm{S}}-\boldsymbol{v}_{\mathrm{L}}|}{\mu_{\mathrm{S}}} \tag{11}$$

where, Re_{S} is particle Reynolds number, d_{S} is particle diameter.

The construction of the Burns turbulent dissipation force model is as follows:

$$\boldsymbol{F}_{\mathrm{Tf}}=C_{\mathrm{TD}}K_{\mathrm{SL}}\frac{D_{\mathrm{L}}}{\sigma_{\mathrm{SL}}}\left(\frac{\nabla\alpha_{\mathrm{S}}}{\alpha_{\mathrm{S}}}-\frac{\nabla\alpha_{\mathrm{L}}}{\alpha_{\mathrm{L}}}\right) \tag{12}$$

where, C_{TD} is the turbulent dispersion coefficient, which is set to 0.6 in this work [11]; D_{L} is the dispersion scalar; and σ_{SL} is the dispersion Prandtl number.

2.3. Turbulence model

As mentioned earlier, RANS is widely applied in solid–liquid simulations within stirred tanks to describe turbulent flow. Recent studies have shown that the RNG k–ε model provides more accurate simulation results [11]. Therefore, this model is employed in the present work. The RNG k–ε model solves two additional transport equations for turbulent kinetic energy (k) and turbulent dissipation rate (ε), as shown below, to calculate the turbulent effective viscosity (μ_{eff}):

$$\frac{\partial}{\partial t}(\rho k)+\frac{\partial}{\partial x_i}(\rho k\boldsymbol{v}_i)=\frac{\partial}{\partial x_j}\left[\mu_{\mathrm{eff}}\alpha_k\frac{\partial k}{\partial x_j}\right]+G_k+G_{\mathrm{b}}-\rho\varepsilon-Y_{\mathrm{M}} \tag{13}$$

$$\frac{\partial}{\partial t}(\rho\varepsilon)+\frac{\partial}{\partial x_i}(\rho\varepsilon \boldsymbol{v}_i)=\frac{\partial}{\partial x_j}\left[\mu_{\text{eff}}\alpha_\varepsilon\frac{\partial\varepsilon}{\partial x_j}\right]+C_{1\varepsilon}\frac{\varepsilon}{k}(G_k+C_{3\varepsilon}G_\text{b})-C_{2\varepsilon}\rho\frac{\varepsilon^2}{k}-R_\varepsilon \tag{14}$$

where, G_k and G_b, represent the generation of turbulence kinetic energy from the mean velocity gradient and buoyancy. Y_M represents the contribution of the fluctuating dilatation in compressible turbulence to the overall dissipation rate. R_ε is a special source term in the ε equation, and its specific definition can be found in the ANSYS Fluent Theory Guide [46]. α_k and α_ε are the inverse effective Prandtl numbers for k and ε. $C_{1\varepsilon}$, $C_{2\varepsilon}$, and $C_{3\varepsilon}$ are constants, with values of 1.42, 1.68, and 1.3, respectively.

2.4. Frictional-kinetic model

Since the conditions in this work involve low rotational speeds, it is necessary to account for particle motion and particle friction. Therefore, the frictional-kinetic model is introduced in this work. The stress between solids is described as the sum of kinetic stress and frictional stress. Consequently, the expressions for solid pressure (P_S) and solid shear viscosity (μ_S) are as follows:

$$P_\text{S}=\begin{cases}P_\text{S}^\text{k} & \alpha_\text{S}<\alpha_{\text{S,min}}\\ P_\text{S}^\text{k}+P_\text{S}^\text{f} & \alpha_\text{S}\geq\alpha_{\text{S,min}}\end{cases} \tag{15}$$

$$\mu_\text{S}=\begin{cases}\mu_\text{S}^\text{k} & \alpha_\text{S}<\alpha_{\text{S,min}}\\ \mu_\text{S}^\text{k}+\mu_\text{S}^\text{f} & \alpha_\text{S}\geq\alpha_{\text{S,min}}\end{cases} \tag{16}$$

The kinetic pressure (P_S^k), frictional pressure (P_S^f), kinetic viscosity (μ_S^k), frictional viscosity (μ_S^f), solid bulk viscosity (λ_S) and transport equation are as follows:

$$P_\text{S}^\text{k}=a_\text{S}\rho_\text{S}\Theta_\text{S}+2\rho_\text{S}(1+e_{\text{ss}})\alpha_\text{S}^2 g_{0,\text{ss}}\Theta_\text{S} \tag{17}$$

$$P_\text{S}^\text{f}=Fr\frac{(\alpha_\text{S}-\alpha_{\text{S,min}})^n}{(\alpha_{\text{S,max}}-\alpha_\text{S})^p} \tag{18}$$

$$\mu_\text{S}^\text{k}=\frac{4}{5}\alpha_\text{S}^2\rho_\text{S}d_\text{S}g_{0,\text{ss}}(1+e_{\text{ss}})\left(\frac{\Theta_\text{S}}{\pi}\right)^{0.5}+\frac{10\rho_\text{S}d_\text{S}\sqrt{\Theta_\text{S}\pi}}{96(1+e_{\text{ss}})g_{0,\text{ss}}}\left[1+\frac{4}{5}g_{0,\text{ss}}\alpha_\text{S}(1+e_{\text{ss}})\right]^2 \tag{19}$$

$$\mu_\text{S}^\text{f}=\frac{P_\text{S}^\text{f}\sin\phi}{2\sqrt{I_{2\text{D}}}} \tag{20}$$

$$\lambda_\text{S}=\frac{4}{3}\alpha_\text{S}^2\rho_\text{S}d_\text{S}g_{0,\text{ss}}(1+e_{\text{ss}})\left(\frac{\Theta_\text{S}}{\pi}\right)^{1/2} \tag{21}$$

$$\frac{3}{2}\left[\frac{\partial}{\partial t}(\alpha_\text{S}\rho_\text{S}\Theta_\text{S})+\nabla\cdot(\alpha_\text{S}\rho_\text{S}\boldsymbol{v}_\text{S}\Theta_\text{S})\right]=-(P_\text{S}\boldsymbol{I}+\nabla\bar{\bar{\tau}}_\text{S}):\nabla\boldsymbol{v}_\text{S}+\nabla\cdot(k_{\Theta_\text{S}}\nabla\Theta_\text{S})-\gamma_{\Theta_\text{S}}+\phi_{\text{LS}} \tag{22}$$

where, Θ_S represents granular temperature; e_{ss} denotes the restitution coefficient, set to 0.95 in this work; $\alpha_{\text{S,max}}$ indicates the solid packing limit, set to 0.63 in this work; $\alpha_{\text{S,min}}$ is the critical volume fraction for friction, set to 0.5 in this work; k_{Θ_S} represents the diffusion coefficient for granular energy; ϕ_{LS} indicates the energy exchange between solid and liquid phases; γ_{Θ_S} denotes the collisional dissipation of energy; $I_{2\text{D}}$ represents the second invariant of the strain rate tensor; ϕ is the angle of internal friction, set to 28.5° in this work; and the coefficients of Fr, n and p are 0.05, 2 and 5, respectively. The definition of the radial distribution function ($g_{0,\text{ss}}$) is as follows:

$$g_{0,\text{ss}}=\left[1-\left(\frac{\alpha_\text{S}}{\alpha_{\text{S,max}}}\right)^{\frac{1}{3}}\right]^{-1} \tag{23}$$

2.5. Dynamic mode decomposition

Since the introduction of DMD in 2009, it has gradually evolved into an advanced data processing tool for identifying dominant modes in transient flow fields within stirred reactors [17,43,49]. This method enables the extraction of the primary dynamic modes in the flow field along with their corresponding characteristic frequencies, which can be ranked and analyzed. Based on these characteristic frequencies, the flow field can be reconstructed at different frequencies, providing insight into the frequency-dependent behavior and characteristics of the flow. In our previous work, DMD was applied to analyze the single-phase turbulent flow field in a multi-shaft stirred reactor, revealing the deep mechanisms of wave–vortex coupling in complex fluid systems, and a wave–vortex coupling model was developed based on these findings. Building on this, this work extends the DMD approach to multiphase flow systems, aiming to identify coherent flow structures at different frequencies and investigate their potential role in enhancing solid–liquid mixing performance. Detailed steps of the DMD algorithm can be found in our earlier works [15].

3. Experimental and Simulation Methods

3.1. Experimental procedure

The experimental setup used in this work is shown in Fig. 1, with the configuration of the three-shaft stirred reactor identical to that in our previous works [14–17]. To achieve better control over the operating conditions of different impellers and

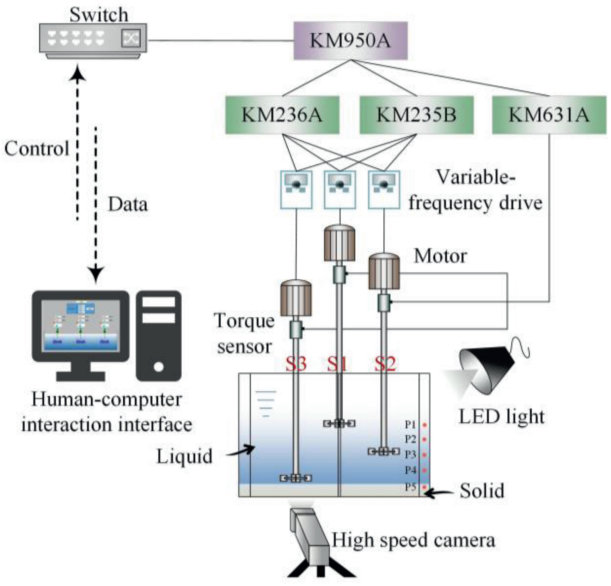

Fig. 1. Experimental setup.

simultaneously collect experimental data, the NT6000 distributed control system (DCS) from SCIYON's (Nanjing Sciyon Wisdom Technology Group Co., Ltd., China) was introduced. This system employs a MODBUS-RTU communication module (KM631A) to acquire torque signals, while the impeller speed and direction are adjusted in real-time through analog input/output modules (KM236A) and digital input/output modules (KM235B). Control is managed *via* a controller unit (KM950A), with commands and data transmission facilitated through a switch connected to the human-machine interface (HMI). During the solid–liquid mixing process, a high-speed camera (model 5F04 M, Revealer, China) is used to capture images, with lighting provided by LED professional film and television lights (model EFIII-200, Jinbei, China) to enhance image quality. Local solid concentration is measured using a sampling method at five sampling positions, from P1 ($Z/H = 1/6$) to P5 ($Z/H = 5/6$).

3.2. Physical parameters

In this work, pure water is used as the liquid phase, with a density of 998.2 $kg \cdot m^{-3}$ and a dynamic viscosity of 1.0×10^{-3} Pa·s. The solid phase consists of custom glass beads, primarily composed of inert silica, with a density of 2580 $kg \cdot m^{-3}$. The particle size distribution and sphericity of the glass beads were measured using the modular particle size and shape analyzer QICPIC-RODOS/L-VIBRI/L from Sympatec GmbH, Germany, as shown in Fig. 2(a) and (b), with a Sauter mean diameter of 169.43 μm and an average sphericity of 0.86. Particle morphology was captured using the modular stereo microscope SteREO Discovery.V20 (ZEISS, Germany), with the image in Fig. 2(c-1) to (c-4) confirming that the majority of the particles are nearly spherical, consistent with the sphericity measurements. A comprehensive analysis of the particle properties used in this experiment provides the basis for the assumption of spherical particles and the setting of particle diameter in subsequent simulations.

3.3. Simulation method

All simulations in this work were performed using ANSYS Fluent 19.2 (Ansys Inc., Canonsburg, PA, USA) on a workstation equipped with an AMD 7950X processor, with a total computation time exceeding 1400 h. The work focuses on the solid–liquid mixing process in a multi-shaft stirred reactor. During the simulation setup, the computational zone within the reactor was divided into stationary zone and rotating zone. The choice of the model for the rotating zone was based on a review of previous works [11,38,40], as well as a balance between computational accuracy and cost, leading to the selection of the multiple reference frame (MRF) model. And a node-matching treatment was applied at the interface between the rotating and stationary regions during meshing to ensure proper transfer of physical quantities. For the reactor walls, bottom, and baffles, no-slip boundary conditions were applied for the liquid phase, while particle–wall collisions were considered for the solid phase, with a particle–wall restitution coefficient of 0.95 and specularity coefficient of 0.25. The turbulence was modeled using the RNG k–ε model, turbulence dissipation with the Burns model, solid stress

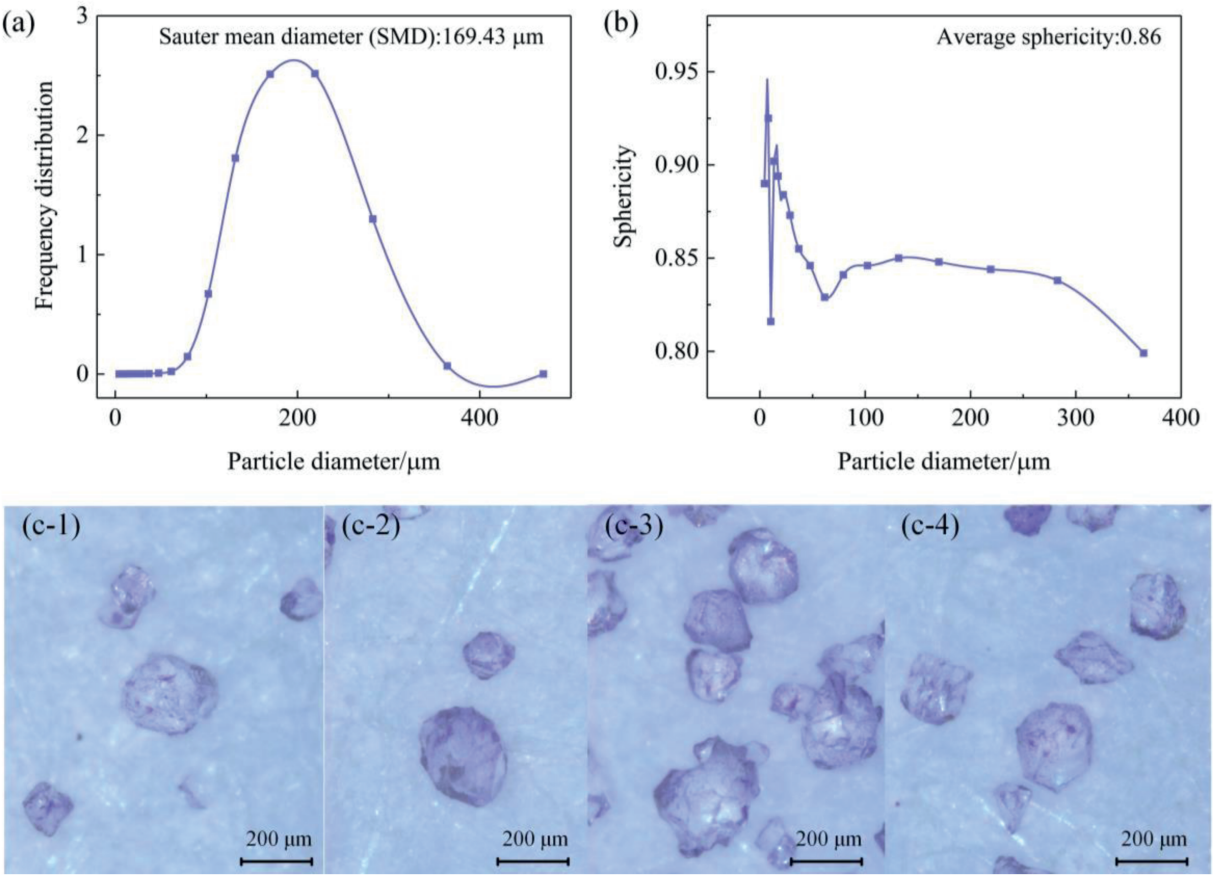

Fig. 2. Analyses of particle physical properties: (a) particle size distribution, (b) sphericity distribution, (c) particle morphology.

with the frictional-kinetic model, and drag was modeled using the Gidaspow model. Further details of these models can be found in the previous chapter. The SIMPLE algorithm was employed for pressure–velocity coupling, and the high-order upwind scheme was used for discretizing the other equations. A convergence criterion of 10^{-5} was set for the transient simulations, with a time step of 0.001 s. The four operating cases were designed by alternately applying reverse rotation (R) and randomized sinusoidal modulation (Sin) to shafts S1, S2, and S3, while keeping the remaining shafts in forward rotation (F) at 90 $r \cdot min^{-1}$. The solid–liquid mixing performance under each operating mode was then evaluated to identify the optimal operating condition. All operational conditions involved in this work are listed in Table 1, and the conditions during the simulation are controlled through a user-defined function (UDF).

3.4. Grid independent test

The grid used in this work was generated using ANSYS ICEM 19.2. Due to the complex structure of the rotating zone, a hybrid grid consisting of tetrahedral and hexahedral cells was employed, as shown in Fig. 3(a). Three grids with total cells counts of 8612125, 10358582, and 12689263 were used for grid independence tests. Under the operating conditions of Case A, the solid velocity and solid volume fraction at different axial positions were compared for the three grids, as shown in Fig. 3(b) and (c). The trends were consistent across all grids. As the grid size increased from 8612125 to 10358582 cells, the average deviations in solid velocity and volume fraction were 2.91% and 2.07%, respectively. When the grid size increased from 10358582 to 12689263 cells, the average deviations in solid velocity and volume fraction were reduced to 1.92% and 1.25%, respectively. Considering both simulation accuracy and computational cost, the grid with 10358582 cells was selected.

3.5. Simulation verification

To assess the accuracy of the numerical calculations, the cloud height, solid volume fraction at different axial positions, and torque were compared between the experimental and simulated results under the operating conditions of Case A. The experimentally acquired solid volume fraction is reported as the means of five independent runs. The experimentally acquired torque signal was sampled at 100 Hz and is reported as the time-series average over each acquisition period. Fig. 4(a-1) to (a-3) show schematic diagrams of the cloud height at 4.0 s for the experiment, and at 3.9 s and 4.0 s for the simulation. The calculated average cloud height in the simulation showed an error of 0.62% compared to the experimental results at 3.9 s, and an error of 11.43% at 4.0 s. The primary reason is a transient lag in achieving solid–liquid dynamic equilibrium at high solids loading. In the experiments, particles are simultaneously influenced by turbulent dispersion and gravitational settling, and intermittent local agglomeration delays the establishment of a stable cloud height. In the current simulations, these microscale agglomeration dynamics are simplified, leading to a better match between the simulated cloud height at 3.9 s and the experimental cloud height at 4.0 s. Fig. 4(b) compares the solid volume fraction at different axial positions after the flow field stabilized. The average error was 5.97%, with a maximum error of 7.76%. Fig. 4(c) shows the comparison of torque between the experiment and simulation, with an average error of 5.63% and a maximum error of 6.56%. These results indicate that the simulation accuracy in this work meets the required standards, thus validating the reliability and precision of the numerical calculations.

4. Results and Discussion

4.1. Solid concentration distribution

For the evaluation of solid–liquid mixing performance, the primary indicator is the solid concentration distribution, with particular emphasis on the axial uniformity of solid concentration. This metric directly reflects the ability of the mixing reactor to lift and suspend solid particles along the axial direction. As shown in Fig. 5, the solid concentration distribution at different axial positions under various operating conditions is depicted. Qualitative results indicate considerable variations in solid particle concentration distribution across different axial positions under different operating conditions. Among the cases, Case D performs the best, followed by Case B and Case C, with Case A showing the poorest performance.

To further investigate the solid concentration distribution, a quantitative analysis was introduced. As shown in Fig. 6(a), the solid volume fraction distribution at different axial positions is presented. The results indicate that, under all operating conditions, the particle volume fraction decreases monotonically with increasing axial position, suggesting that gravity plays a significant role in the mixing and distribution of particles under these conditions. Furthermore, it is noteworthy that a concentration inflection point appears around the axial position $Z/H = 0.5$ for all operating conditions. This phenomenon indicates that, for this configuration of multi-axis stirred reactors, this position corresponds to the vortex center in the flow field, where the particle behavior transitions from being predominantly suspended to sedimentation-dominated, as previously identified in our research [14].

Further quantification of the concentration gradient ratio from the bottom to the top of the flow field reveals the following values for the four operating conditions: 28.3, 10.6, 14.9, and 4.4. Taking Case D as the baseline, the concentration gradient ratios for the other three operating conditions increased by 543.18%, 140.91%, and 238.64%, respectively. This suggests that Case A exhibits significant particle accumulation at the bottom, while Case B and Case C show some improvements, yet still experience particle back-mixing at the top. In contrast, Case D demonstrates a more efficient mixing process. To further quantify this concentration distribution and effectively assess the mixing performance, a concentration decay model was established using the bottom concentration ($\alpha_{S,0}$) as a reference value, as described below:

Table 1
Summary of operating conditions in this work.

Specification	S1	S2	S3
Case A	90 (F)	90 (F)	90 (F)
Case B	$10\sin(0.2t) + 90$ (R)	90 (F)	90 (F)
Case C	90 (F)	$10\sin(0.2t) + 90$ (R)	90 (F)
Case D	90 (F)	90 (F)	$10\sin(0.2t) + 90$ (R)

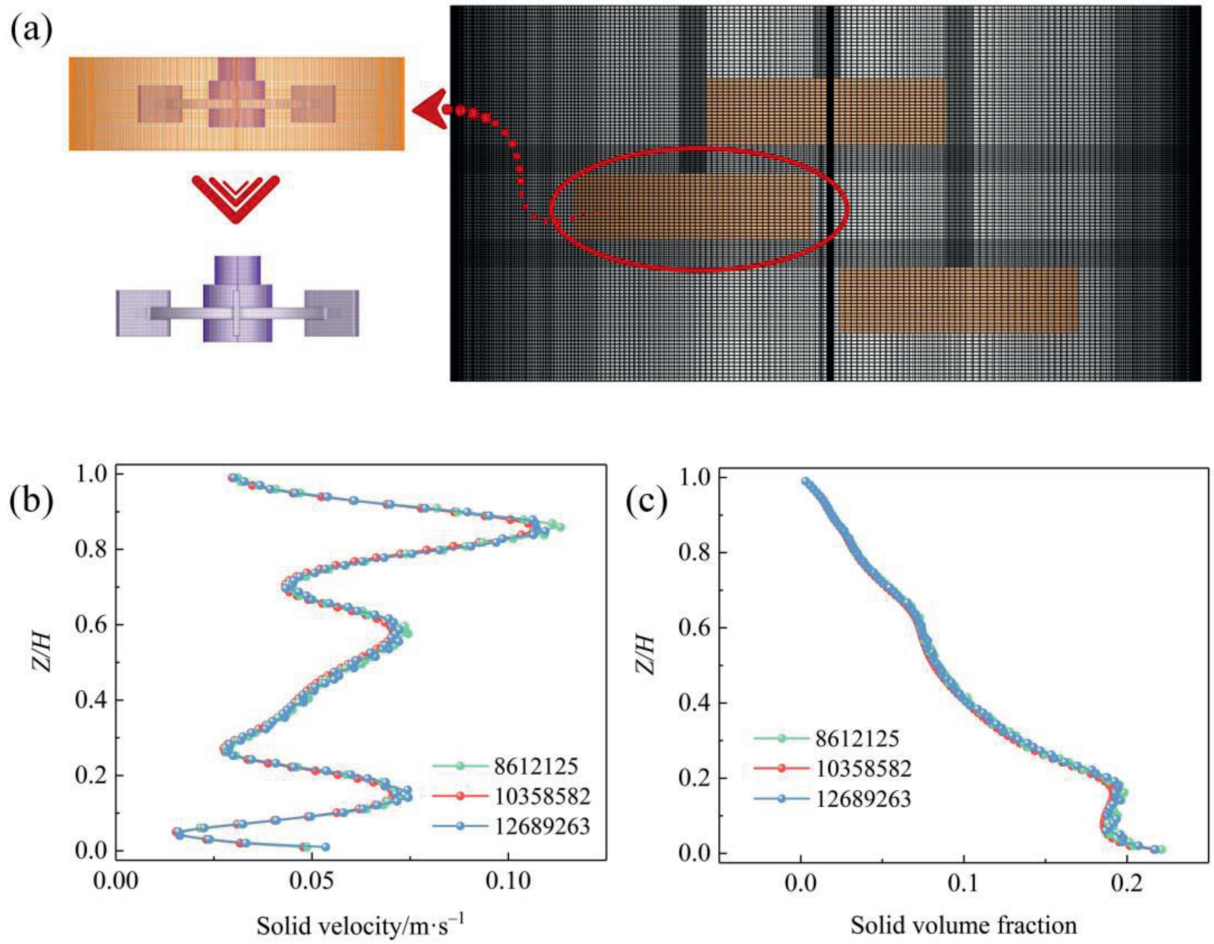

Fig. 3. Grid independence verifications: (a) grid schematic, (b) comparisons of solid velocity at different axial positions for different grids, (c) comparisons of solid volume fraction at different axial positions for different grids.

$$\alpha_{S,Z/H} = \alpha_{S,0} e^{-k_S(Z/H)} \tag{24}$$

The axial distribution of solid volume fraction under four different operating conditions was coupled using a concentration decay model, ensuring a goodness of fit (R^2) greater than 0.985, with the decay coefficient (k_S) for each condition being 4.25, 2.92, 3.18, and 1.82, respectively. Taking Case D as the baseline, k_S increased by 133.52%, 60.44%, and 74.73% for the other three operating conditions. In the solid–liquid mixing process within the stirred reactor, the competition between particle sedimentation (downward) and turbulent diffusion (upward) plays a dominant role, with the mixing performance largely depending on the relative magnitudes of these two effects. k_S serves as an indicator of the relative rates of sedimentation and diffusion. Clearly, Case A is predominantly controlled by sedimentation, while Cases B and C are in a state of competition between sedimentation and diffusion. In contrast, Case D is dominated by turbulent upward diffusion. The homogeneity of solid mixing is also critical in the solid–liquid mixing process, as it directly reflects the mixing performance of the reaction. Therefore, this work introduces the concept of solid homogeneity (σ) to further evaluate the mixing efficiency:

$$\sigma = 1 - \sqrt{\frac{\sum_{n}^{1} \left(\alpha_S - \alpha_{S,ave}\right)^2}{n}} \tag{25}$$

As shown in Fig. 6(b), the solid homogeneity under different operating conditions is compared. Case D consistently exhibits superior performance, with homogeneity values improved by 3.22%, 2.81%, and 2.74% relative to Cases A, B, and C, respectively. These results highlight the enhanced mixing efficiency achieved in Case D, where solid particles are more effectively suspended and uniformly distributed throughout the reactor.

4.2. Cloud height and radial solid concentration distribution

Furthermore, this work presents iso-surface plots of cloud height under different operational conditions, as illustrated in Fig. 7. The results indicate that in Case A, there is a pronounced phenomenon of solid deposition at the bottom, particularly evident in the baffle region. In contrast, Cases B and C exhibit similar cloud height distributions, which are consistent with the previous axial solid concentration analysis. Both cases demonstrate significant stratification, indicating obstruction in the axial transport of solid particles. Conversely, Case D shows the weakest bottom deposition phenomenon, with no noticeable stratification among the cloud heights of different solid concentrations. Instead, there is a trend of mutual mixing, suggesting more vigorous movement of solid particles and smoother axial transport.

To further highlight the differences under various operational conditions, this work characterizes the solid concentration distribution along the radial cross-section through the S3 shaft, as shown in Fig. 8. The results indicate that Cases A, B, and C exhibit significant particle sedimentation at the bottom, and there are large regions of low solid concentration at the top of the flow field,

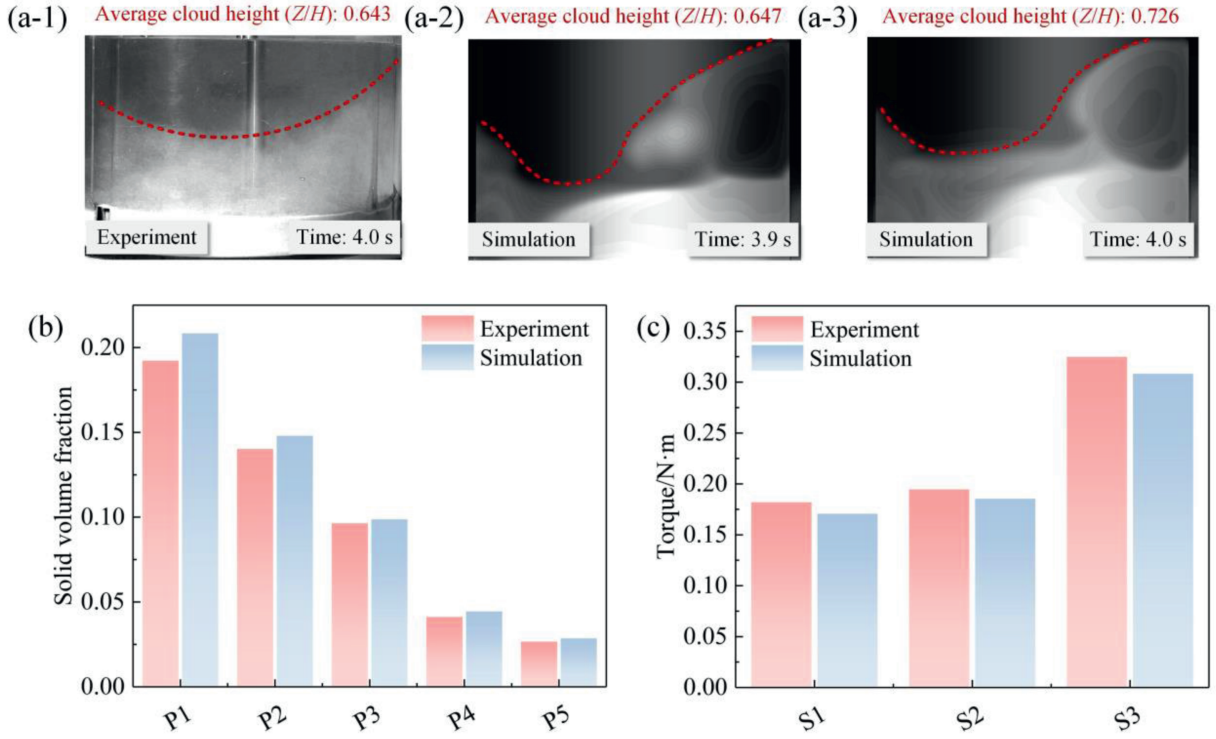

Fig. 4. Simulation verifications: (a) comparisons of cloud height between experimental and simulated results, (b) comparisons of solid volume fraction at different axial positions between experimental and simulated results, (c) comparisons of torque between experimental and simulated results.

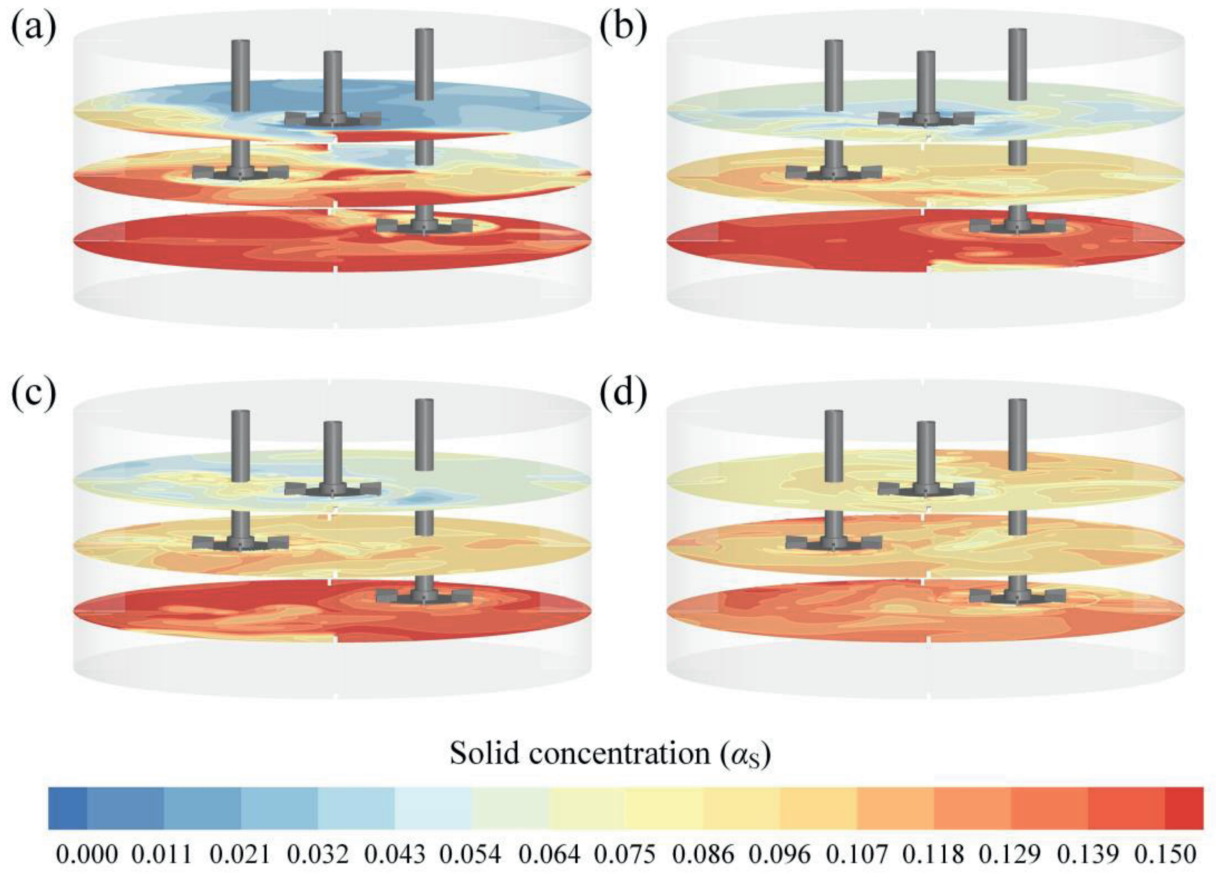

Fig. 5. Solid concentration distributions at different axial positions: (a) Case A, (b) Case B, (c) Case C, (d) Case D.

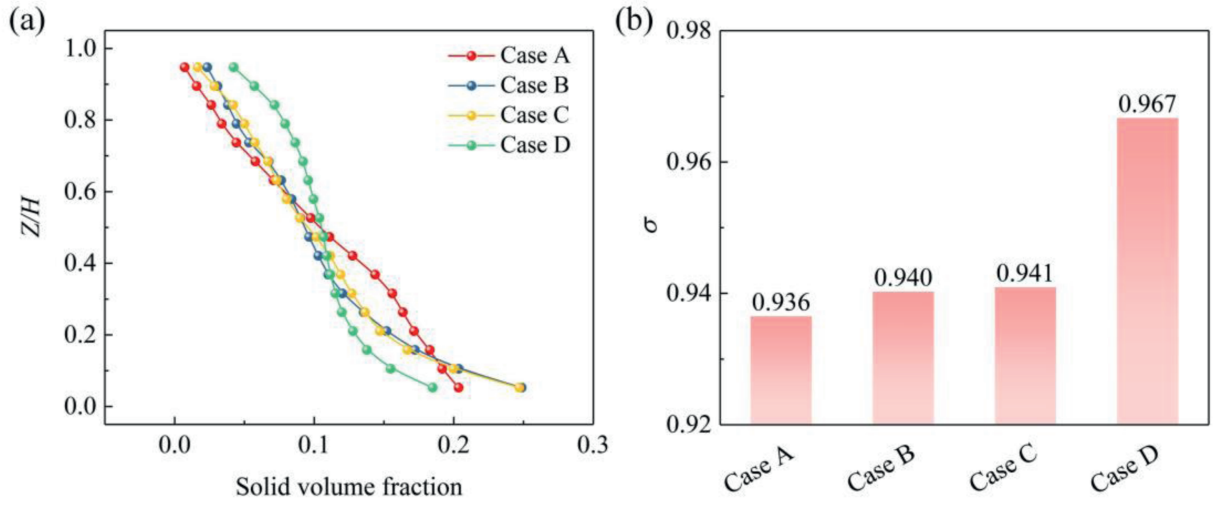

Fig. 6. Quantitative analyses of solid concentration distribution: (a) variation of solid volume fraction with axial position under different operating conditions, (b) solid homogeneity under different operating conditions.

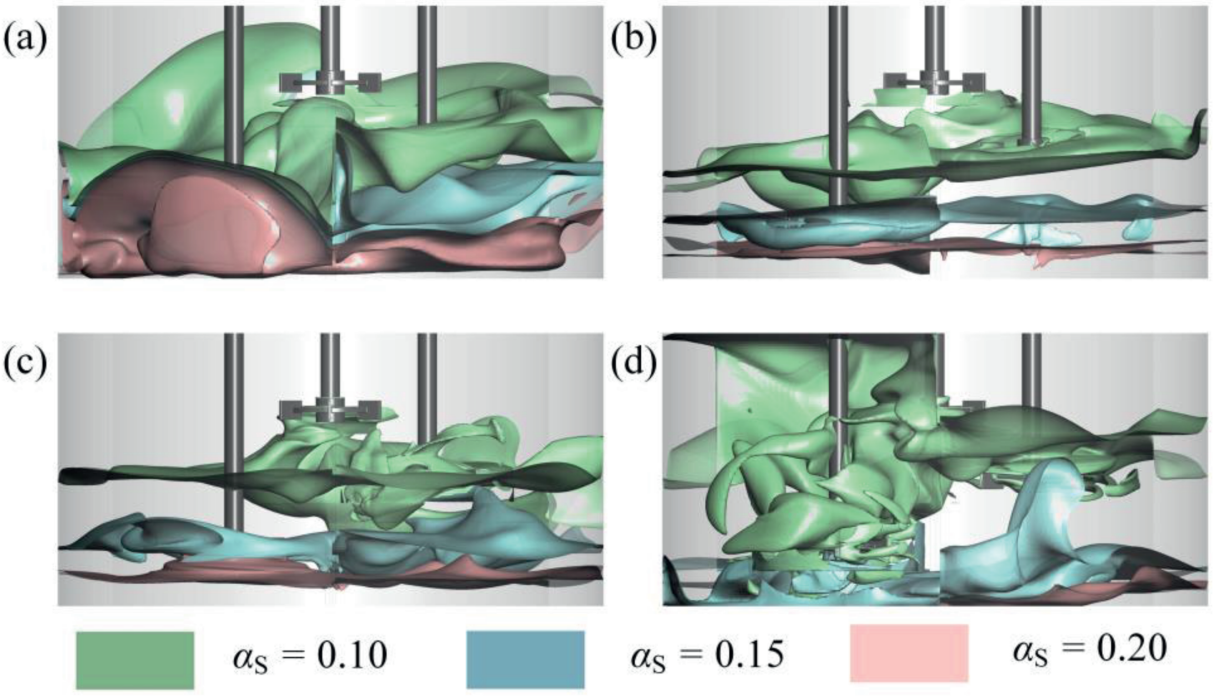

Fig. 7. Cloud heights under different operational conditions: (a) Case A, (b) Case B, (c) Case C, (d) Case D.

particularly noticeable in Case A. Additionally, these cases display substantial axial concentration gradients, indicating rapid energy decay for axial particle transport and insufficient axial lifting force. In contrast, Case D shows only a small area of high solid concentration near the bottom, away from the impeller region, with a more uniform solid concentration distribution throughout the flow field. In summary, Case D demonstrates superior solid–liquid mixing performance, suggesting that applying chaotic rotational speeds to the bottom impellers to enhance the axial lifting force of solid particles is an effective strategy in multi-shaft stirred reactors. The underlying reasons are related to the evolution of the flow field structure. The subsequent sections of this work will focus on the analysis of flow field structures and the elucidation of coupling enhancement mechanisms at different scales.

4.3. Analysis of flow field

The streamlines and liquid velocity contour maps under different operating conditions are shown on Fig. 9. From the overall flow field structure, significant differences can be observed across the various operating conditions. The flow field structure in Case A is relatively simple, with localized complex vortex structures appearing near the impeller and in the central region of the flow field. High-velocity regions are mainly concentrated around the impeller and near the walls. In contrast, Cases B and C, which apply chaotic rotation speeds to shafts S1 and S2, exhibit more complex flow field structures in these regions, accompanied by the emergence of high-velocity zones. Case D, on the other hand, presents a complex flow field structure throughout, characterized

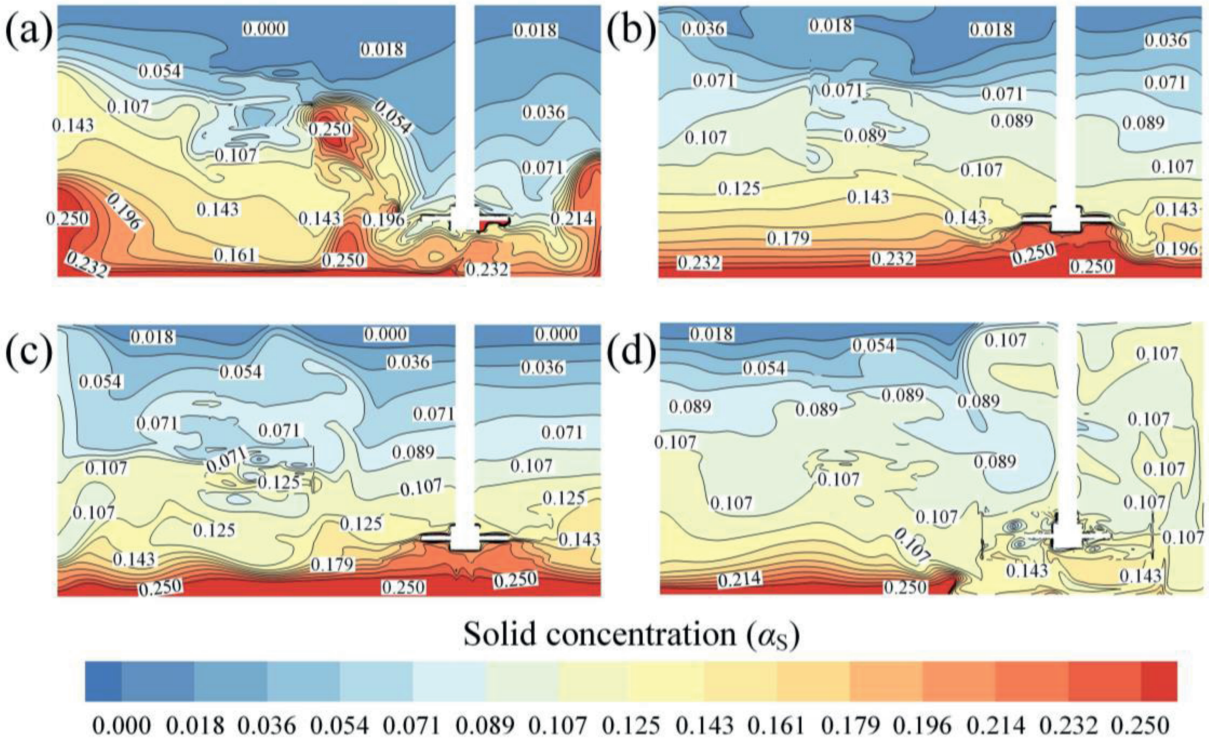

Fig. 8. Radial cross-sectional solid concentration distributions under different operational conditions: (a) Case A, (b) Case B, (c) Case C, (d) Case D.

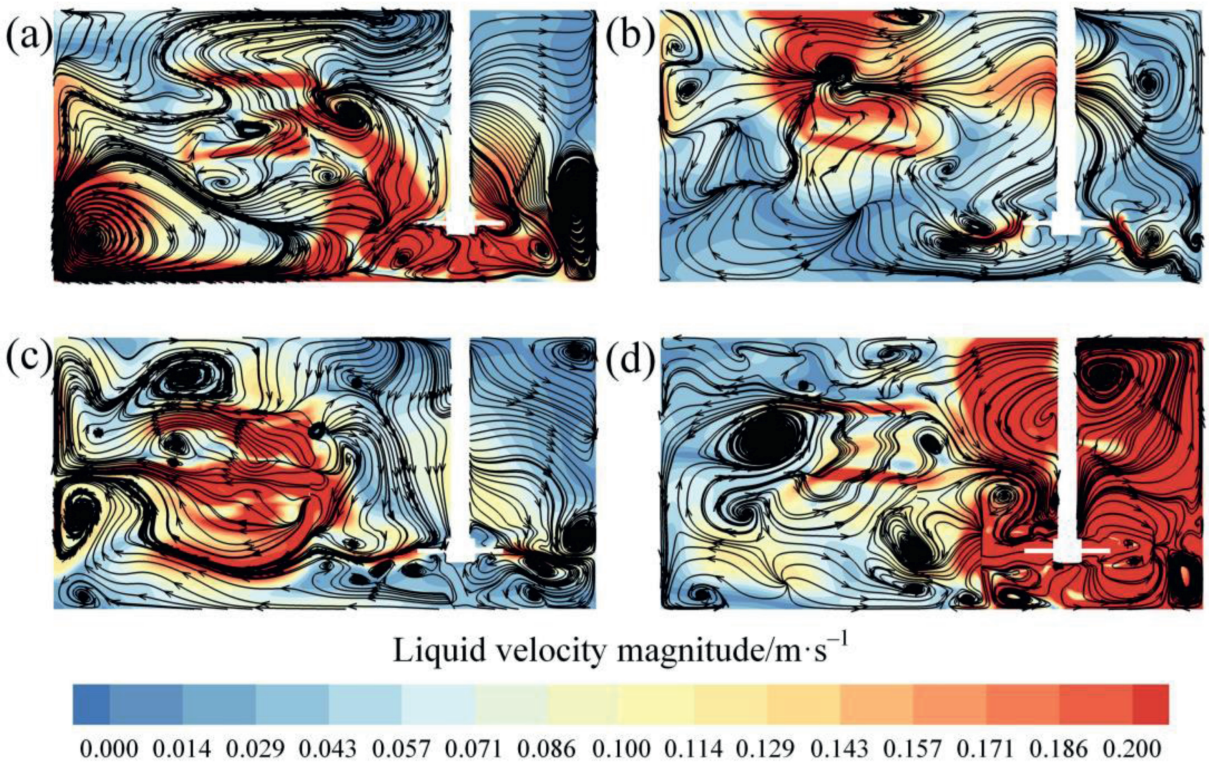

Fig. 9. Flow field characteristics under different operating conditions: (a) Case A, (b) Case B, (c) Case C, (d) Case D.

by the interaction of vortices of different scales, with high-velocity regions extending from the bottom of the impeller upwards, not confined to a specific area, thus facilitating rapid axial transport of solid particles. The study of axial liquid velocity distribution is also crucial. Fig. 10 shows the axial fluid velocity distribution contours under different operating conditions. Clearly, Case D has an overall higher axial liquid velocity, with regions of opposing flow directions appearing in pairs, indicating a more complete axial mass

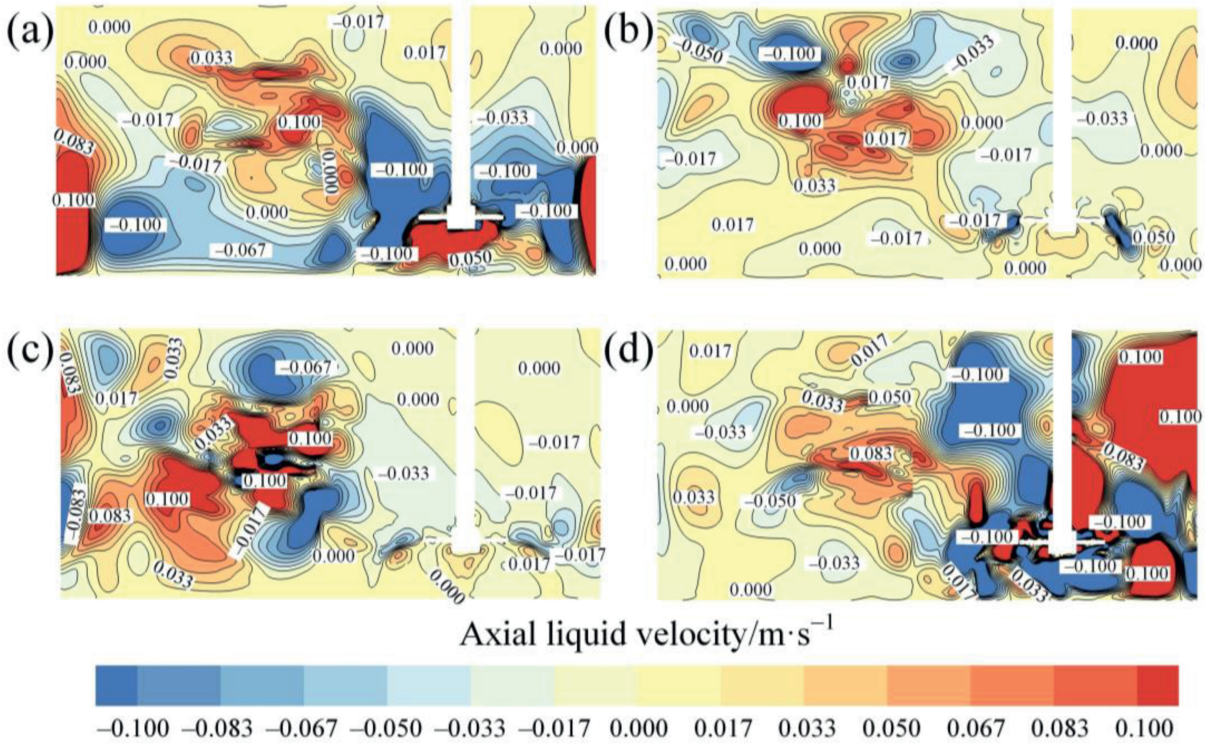

Fig. 10. Axial liquid velocity distribution contours under different operating conditions: (a) Case A, (b) Case B, (c) Case C, (d) Case D.

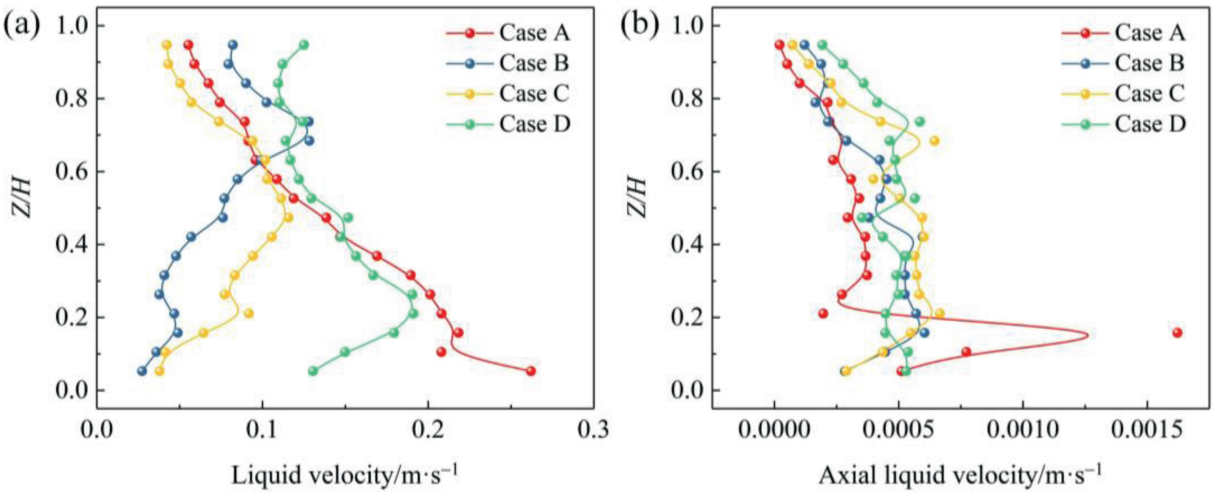

Fig. 11. Variation of velocity with axial position under different operating conditions: (a) liquid velocity, (b) axial liquid velocity.

transfer pathway, which is beneficial for the mixing of solid particles. In contrast, Case A exhibits a large area of low axial liquid velocity at the bottom of the flow field, explaining the severe sedimentation of solid particles. Cases B and C have large areas with zero axial liquid velocity, leading to an overall mixing performance that does not significantly improve.

Additionally, this work quantitatively analyzed the variation of liquid velocity and axial liquid velocity with axial position, as shown in Fig. 11. The results indicate that Case D exhibits significantly superior flow field stability and energy transfer efficiency. Firstly, compared with Case A (0.141 ± 0.063), Case B (0.072 ± 0.031), and Case C (0.072 ± 0.026), Case D maintains a relatively high global fluid velocity while exhibiting the smallest velocity fluctuation across the reactor (0.134 ± 0.026). Moreover, the coefficient of variation in Case D is only 0.190, substantially lower than in Case A (0.407), Case B (0.418), and Case C (0.327), indicating a more uniform velocity distribution and a markedly reduced energy dissipation rate, which is beneficial for improving mixing efficiency and enhancing mass transfer. Additionally, the fluctuation amplitude of the axial fluid velocity in Case D is only 0.43, compared with 1.01 in Case A, 0.83 in Case B, and 1.12 in Case C, indicating a more stable flow field, reduced axial back-mixing, and an optimized axial distribution of solid particles.

4.4. Analysis of DMD

From the previous analysis, it is evident that the evolution of the flow field structure is a critical factor influencing solid–liquid

mixing performance. Specifically, the flow field instability induced by nonlinear interactions among vortices of different scales plays a significant role in enhancing solid–liquid mixing efficiency. To further analyze the enhancement mechanism of solid–liquid mixing performance due to multi-scale coupling in the flow field, this work conducted DMD analysis under different operating conditions, with the results shown in Fig. 12. It should be noted that DMD separates structures associated with a single frequency and their corresponding growth/decay rates and ranks them. As is well known in turbulent systems, vortex scale is inversely proportional to characteristic frequency [50]. Therefore, drawing on previous studies and remaining consistent with prior work, and for the convenience of subsequent analysis, vortices of different scales were defined according to their modal properties [15,17,42,43,49]. The results indicate significant differences in the distribution and aggregation of vortices of different scales under various operating conditions. Specifically, in Cases A, B, and C, vortices of different scales primarily exhibit local aggregation. Understandably, in Cases B and C, vortices of different scales are mainly concentrated near the impellers with chaotic rotational speeds. However, in Case A, vortices of different scales significantly aggregate at the bottom of the vessel and the bottom impeller region, due to changes in flow field characteristics caused by solid particle deposition at the bottom, leading to highly concentrated energy dissipation in this area, which drives local vortex aggregation. Case D, on the other hand, exhibits distinctly different flow field characteristics: vortices of different scales are widely distributed throughout most of the flow field and exhibit an interwoven structure. From the perspective of streamlines, the intense multi-scale vortex interactions (manifested as highly entangled streamlines) in Cases B and C remain primarily confined to the vicinity of the impellers with chaotic rotational speeds. In contrast, Case A shows stronger multi-scale streamline entanglement intensity in localized areas (the bottom of the vessel) compared to the former two. However, in the upper space of the flow field, such vortex interactions are significantly reduced. In Case D, uniformly intense multi-scale streamline entanglement is observed throughout the entire flow field, indicating a more

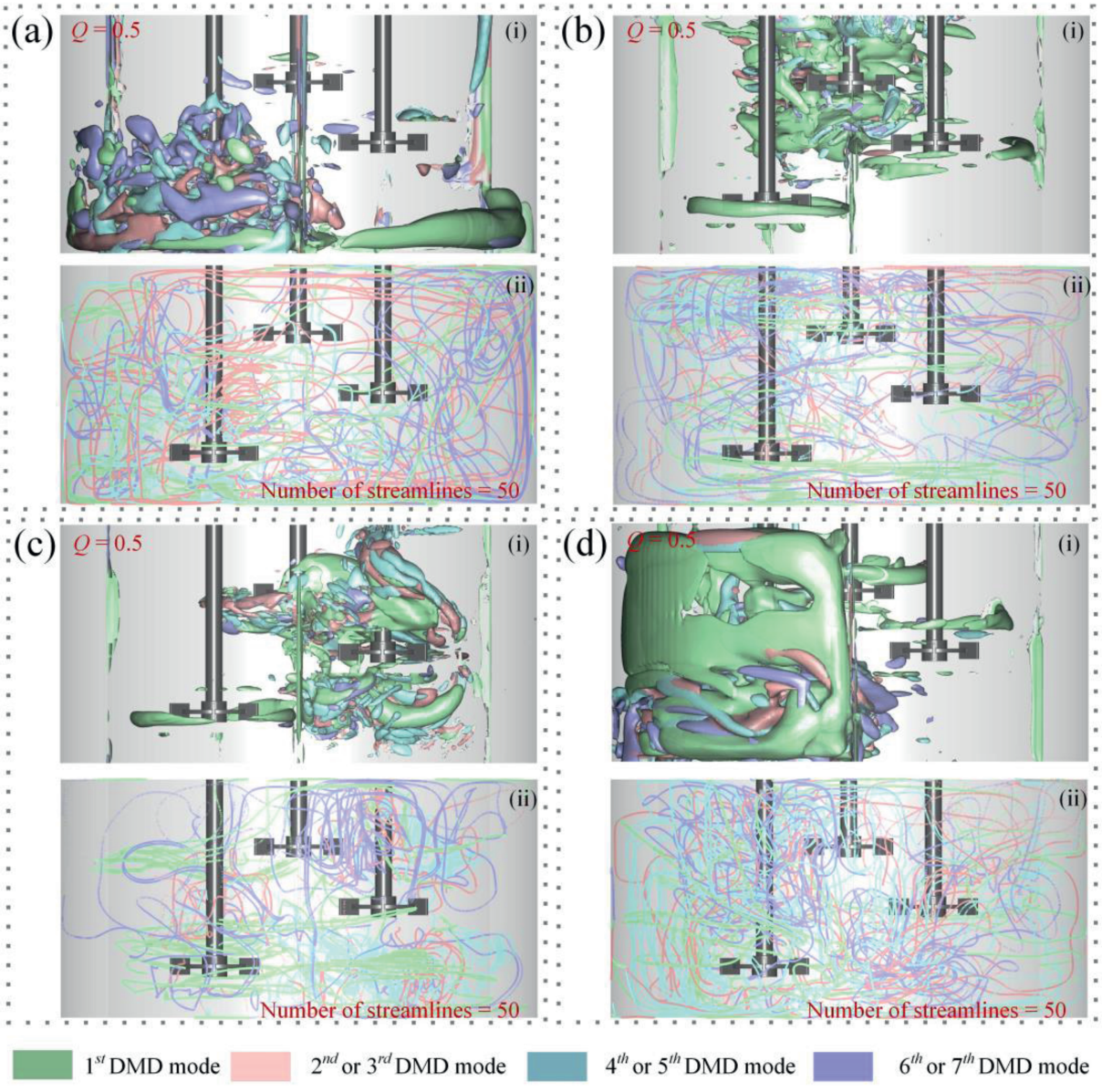

Fig. 12. Results of DMD analysis: (a) Case A, (b) Case B, (c) Case C, (d) Case D. Note: (i) Iso-surface of *Q*-criterion, (ii) 3D streamlines.

spatially uniform distribution of multi-scale vortex interactions, which is more conducive to the uniform distribution of solid particles within the flow field. Nevertheless, the aforementioned analysis of the enhancement mechanism of solid–liquid mixing performance due to multi-scale vortex interweaving and coupling remains primarily qualitative and requires further quantitative research.

4.5. Multi-scale vortex coupling analysis

To delve into the dynamic coupling mechanisms between multi-scale vortex structures and their impact on enhanced solid–liquid mixing performance, this work employs the method previously developed by our team to conduct a time series analysis of the modal coefficients under different operating conditions [15], as shown in Fig. 13. Across various conditions, the modal coefficients exhibited oscillatory decay over time, primarily attributed to energy cascade effects induced by the coupling and nesting of vortex structures of different scales.

To quantitatively characterize the intensity and features of dynamic vortex coupling, this work fitted the time series of modal coefficients with a complex exponential function: $a\exp(-bt)(\cos(ct+d)+i\sin(ct+d))$. During the fitting process, this work strictly controlled the root mean square error (RMSE) to be less than 0.01 to ensure fitting accuracy. Here, b (the decay/growth rate of modal amplitude) and c (the angular frequency of modal oscillation) are key parameters for quantitatively characterizing the intensity and pattern of dynamic coupling between different vortex scales. The quantitative analysis results are summarized in Tables 2 and 3. Among all operating cases, Case D exhibited the lowest decay rate, particularly achieving a minimum value of 0.0619 in the 6th & 7th modes. Concurrently, Case D demonstrated higher frequencies in the 6th & 7th modes as well as the 8th & 9th modes. This low decay-high frequency oscillation characteristic effectively optimizes the energy cascade path, avoiding local dissipation phenomena observed in Cases B and C, and the dead zones observed in Case A. Consequently, Case D significantly enhances global uniformity and diffusion efficiency in solid–liquid mixing. Furthermore, the smallest frequency difference between adjacent scales in Case D, among the four operating conditions, significantly reduces the resistance to energy cascade, inducing resonance effects and forming a self-sustaining energy cycle. This leads to enhanced overall solid–liquid mixing uniformity without local high-energy dissipation. Based on this, this work summarizes the multi-scale vortex cooperative control mechanism to enhance solid–liquid mixing in multi-shaft mixers by varying rotational speeds:

- Large-scale vortices (2nd & 3rd modes): These act as the drivers of the macroscopic flow field and should avoid high-frequency disturbances that could disrupt the macroscopic flow field, thereby providing a stable carrier for nested structures.

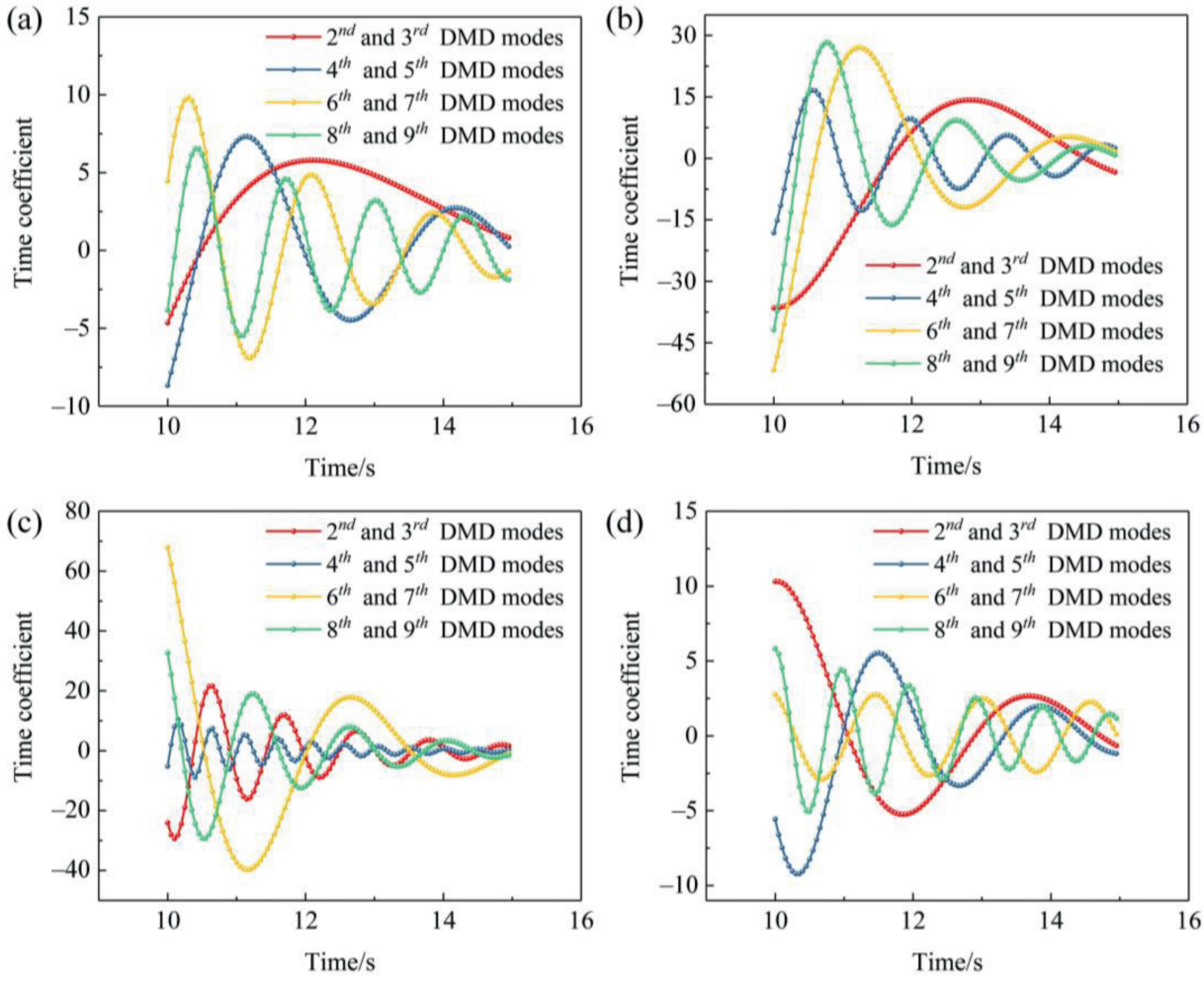

Fig. 13. Real part of DMD mode coefficients: (a) Case A, (b) Case B, (c) Case C, (d) Case D.

Table 2
Fitted results of parameter *b* under different operating conditions.

Specification	2nd and 3rd	4th and 5th	6th and 7th	8th and 9th
Case A	0.3917	0.3242	0.3916	0.2761
Case B	0.3320	0.3847	0.5383	0.5918
Case C	0.5663	0.6697	0.5326	0.6139
Case D	0.3695	0.4356	0.0619	0.2846

Table 3
Fitted results of parameter *c* under different operating conditions.

Specification	2nd and 3rd	4th and 5th	6th and 7th	8th and 9th
Case A	0.6208	2.0698	3.5257	4.8513
Case B	1.1097	4.4685	2.0673	3.3456
Case C	5.9606	12.9954	2.1023	4.4649
Case D	1.7155	2.6783	4.0322	6.4703

- Medium-scale vortices (4th & 5th modes): Serving as energy transfer hubs, these need to improve the frequency matching of adjacent scale vortices and moderate energy decay to achieve efficient energy transfer.
- Small-scale vortices (6th & 7th modes and 8th & 9th modes): Acting as the executors of micro-mixing, these need to achieve low decay and high frequency, inducing resonance effects in adjacent scale vortices, thereby achieving sustained mixing of solid particles and enhancing overall solid–liquid mixing performance.

Understanding and applying the above multi-scale synergistic nesting chaos-enhanced mechanism can achieve enhanced solid–liquid mixing performance in multi-shaft stirred reactors by further optimizing operating conditions.

5. Conclusions

This work aims to explore the enhancement pathways of solid–liquid mixing processes within multi-shaft stirred reactors. The core objectives include identifying the optimal shaft for variable speed control based on solid–liquid mixing performance indicators and elucidating the dynamic coupling mechanisms of multi-scale vortex structures induced by operational condition changes, along with their synergistic enhancement effects. The main conclusions are as follows:

1. By employing the RNG k–ε model coupled with the EE-KTGF model, this work achieved numerical simulation of the solid–liquid mixing process in multi-shaft stirred reactors. The simulation results align well with experimental data, confirming the suitability of this method for accurate predictions in large-scale multi-shaft reactors.
2. Comparison of mixing performance across four conditions showed that, with Case D as the reference, other conditions exhibited an increase in solid concentration gradient by 140.91% to 543.18% and an enhancement in particle settling rate by 60.44% to 133.52%. The solid homogeneity in Case D improved significantly by 2.74% to 3.22%, indicating that variable speed control of the bottom impeller can optimize particle suspension distribution and enhance overall mixing performance.
3. Flow field analysis shows that Case D mitigates excessive local velocities and yields a more uniform global velocity distribution (coefficient of variation of 0.190, markedly lower than in Cases A–C). Its axial velocity fluctuation amplitude (0.43) is the lowest among all cases, indicating enhanced flow-field stability, reduced axial back-mixing, and an optimized axial distribution of particles.
4. DMD analysis of the flow field and its modal time series indicated that the mixing enhancement mechanism in Case D stems from: large-scale vortices avoiding high-frequency disturbances to maintain macroscopic flow field stability; mid-scale vortices improving cross-scale frequency matching and regulating moderate energy dissipation; small-scale vortices achieving low attenuation rates and high-frequency oscillations, thereby exciting cross-scale resonance effects; and multi-scale synergistic nesting chaos-enhancing continuous solid–liquid mixing.

In summary, this work identifies variable-speed control of the bottom impeller as an optimal route for enhancing solid–liquid mixing and elucidates a multi-scale, synergistic, chaos-enhanced mechanism of “macroscopic stability–mesoscopic matching–microscopic resonance”. These findings provide a theoretical foundation for the design and operational optimization of multi-shaft stirred reactors. The strategy is particularly promising for high solid-content systems such as mineral processing and bio-fermentation. Moreover, machine-learning methods can be leveraged to further optimize solid–liquid mixing in multi-shaft stirred reactors, enabling model-based design, real-time monitoring, and industrial-scale prediction and control of inter-shaft interference [51,52].

CRediT Authorship Contribution Statement

Tong Meng: Writing – original draft, Visualization, Software, Methodology, Data curation, Conceptualization. Yu Wang: Investigation, Data curation. Yijuan Tian: Investigation, Data curation. Shuang Qin: Software, Formal analysis. Yuyan Lin: Investigation. Peiqiao Liu: Investigation. Yundong Wang: Writing – review & editing, Methodology. Zuohua Liu: Supervision, Resources, Methodology, Funding acquisition.

Data Availability

The original data that support the findings of this study are available on request from the corresponding author.

Declaration of Competing Interest

The authors declare that they have no known competing financial interests or personal relationships that could have appeared to influence the work reported in this paper.

Acknowledgements

This work was supported by the Chongqing Natural Science Foundation Innovation and Development Joint Fund Project (CSTB2022NSCQ-LZX0014) and Fundamental Research Funds for Central Universities (2022CDJQY-005, 2023CDJXY-047). At the same time, this work also received funding from the China Scholarship Council and Young Elite Scientists Sponsorship Program for Doctoral Students by the China Association for Science and Technology (CAST) to Tong Meng. We would like to extend our heartfelt gratitude to Dr. Xiaofei Wei from Chongqing University for her invaluable suggestions and all the efforts she has put into this work.

References

[1] H. Chen, B. Ouyang, X.G. Yi, X.B. Zhang, Z.H. Luo, Insights into the impact of small particle liquid film on the spatiotemporal distribution of suspension in stirred reactors, *Ind. Eng. Chem. Res.* 63 (30) (2024) 13379–13388.

[2] X.L. Li, H.L. Zhao, Z.M. Zhang, Y. Liu, T.A. Zhang, Numerical optimization for blades of intermig impeller in solid–liquid stirred tank, *Chin. J. Chem. Eng.* 29 (2021) 57–66.

[3] L. Torrente-Murciano, J.B. Dunn, P.D. Christofides, J.D. Keasling, S.C. Glotzer, S. Y. Lee, K.M. van Geem, J. Tom, G.H. He, The forefront of chemical engineering research, *Nat. Chem. Eng.* 1 (1) (2024) 18–27.

[4] V.M. Barabash, R.S. Abiev, N.N. Kulov, Theory and practice of mixing: a review, *Theor. Found. Chem. Eng.* 52 (4) (2018) 473–487.

[5] P. Mishra, F. Ein-Mozaffari, Using computational fluid dynamics to analyze the performance of the maxblend impeller in solid–liquid mixing operations, *Int. J. Multiphas. Flow* 91 (2017) 194–207.

[6] D.Y. Gu, Y.H. Song, H. Xu, L. Wen, M. Ye, CFD simulation and experimental analysis of solid–liquid mixing characteristics in a stirred tank with a self-similarity impeller, *J. Taiwan Inst. Chem. Eng.* 146 (2023) 104878.

[7] A. Kazemzadeh, F. Ein-Mozaffari, A. Lohi, Effect of impeller type on mixing of highly concentrated slurries of large particles, *Particuology* 50 (2020) 88–99.

[8] Z.W. Chen, Y.J. Wu, J. Wang, P.C. Luo, Study on the solid–liquid suspension behavior in a tank stirred by the long-short blades impeller, *Chin. J. Chem. Eng.* 47 (2022) 79–88.

[9] X. Xiong, Z.H. Liu, C.Y. Tao, Y.D. Wang, F.Q. Cheng, H. Li, Reduced power consumption in stirred vessel with high solid loading by equipping punched baffles, *Chin. J. Chem. Eng.* 56 (2023) 203–214.

[10] B.Q. Liu, Z.L. Xu, F.Y. Fan, B.L. Huang, Experimental study on the solid suspension characteristics of coaxial mixers, *Chem. Eng. Res. Des.* 133 (2018) 335–346.

[11] Z.L. Xu, C. Yang, Z.Q. Zhang, B.Q. Liu, Z.J. Jin, Study on the numerical model of dense solid suspension driven by a coaxial mixer, *Ind. Eng. Chem. Res.* 60 (4) (2021) 1939–1951.

[12] L. Zhang, K. Yang, M. Li, Q.T. Xiao, H. Wang, Enhancement of solid–liquid mixing state quality in a stirred tank by cascade chaotic rotating speed of main shaft, *Powder Technol.* 397 (2022) 117020.

[13] F. Maluta, F. Alberini, A. Paglianti, G. Montante, A CFD study on the change of scale of Non-Newtonian stirred digesters at low Reynolds numbers, *Chem. Eng. Res. Des.* 205 (2024) 498–509.

[14] T. Meng, Y. Wang, S.S. Wang, S. Qin, Q. Zhang, Y.D. Wang, C.Y. Tao, Y.Q. Xu, Z. H. Liu, Exploration of multishafts stirred reactors: an investigation on experiments and large eddy simulations for turbulent chaos and mixing characteristics, *Ind. Eng. Chem. Res.* 63 (5) (2024) 2441–2456.

[15] T. Meng, Y. Wang, S. Qin, P.Q. Liu, Y.D. Wang, C.Y. Tao, Z.H. Liu, Complex flow field analysis in multi-shaft stirred reactors: dynamics of wave–vortex coupling revealed by POD and DMD methods, *Chem. Eng. Sci.* 301 (2025) 120753.

[16] T. Meng, J. Yang, S.S. Wang, Y. Wang, S. Qin, Y.D. Wang, C.Y. Tao, Q. Zhang, Z.H. Liu, Multi-shaft stirred reactors mixing efficiency: rapid characterization strategy based on chaotic attractors, *AIChE J.* 70 (10) (2024) e18510.

[17] T. Meng, Y. Wang, S. Qin, P.Q. Liu, Q. Zhang, Y.D. Wang, C.Y. Tao, Z.H. Liu, From patterns to cocktails: a novel visualization method for turbulent flow fields in stirred reactors, *Ind. Eng. Chem. Res.* 63 (44) (2024) 19320–19328.

[18] S.S. Wang, T. Meng, Q. Zhang, C.Y. Tao, Y.D. Wang, Z.Q. Li, Z.H. Liu, A strategy for strengthening chaotic mixing of dual shaft eccentric mixers by changing Non-Newtonian fluids kinetic energy distribution, *Chin. J. Chem. Eng.* 69 (2024) 122–134.

[19] G.R. Kasat, A.R. Khopkar, V.V. Ranade, A.B. Pandit, CFD simulation of liquid-phase mixing in solid–liquid stirred reactor, *Chem. Eng. Sci.* 63 (15) (2008) 3877–3885.

[20] S.F. Wright, I. Zadrazil, C.N. Markides, A review of solid–fluid selection options for optical-based measurements in single-phase liquid, two-phase liquid–liquid and multiphase solid–liquid flows, *Exp. Fluid* 58 (9) (2017) 108.

[21] S. Wiederseiner, N. Andreini, G. Epely-Chauvin, C. Ancey, Refractive-index and density matching in concentrated particle suspensions: a review, *Exp. Fluid* 50 (5) (2011) 1183–1206.

[22] M. Sharifi, B. Young, Review of applications of electrical resistance tomography to chemical engineering, *Rev. Chem. Eng.* 39 (4) (2023) 567–599.

[23] C. Poelma, Ultrasound imaging velocimetry: a review, *Exp. Fluid* 58 (1) (2016) 3.

[24] S.J. Li, L.T. Zhu, X.B. Zhang, Z.H. Luo, Recent advances in CFD simulations of multiphase flow processes with phase change, *Ind. Eng. Chem. Res.* 62 (28) (2023) 10729–10786.

[25] S. Hosseini, D. Patel, F. Ein-Mozaffari, M. Mehrvar, Study of solid–liquid mixing in agitated tanks through computational fluid dynamics modeling, *Ind. Eng. Chem. Res.* 49 (9) (2010) 4426–4435.

[26] P.Y. Shi, R. Rzehak, Solid–liquid flow in stirred tanks: euler–euler/rans modeling, *Chem. Eng. Sci.* 227 (2020) 115875.

[27] R.S.S. Raja Ehsan Shah, B. Sajjadi, A.A. Abdul Raman, S. Ibrahim, Solid–liquid mixing analysis in stirred vessels, *Rev. Chem. Eng.* 31 (2) (2015) 119–147.

[28] S. Subramaniam, S. Balachandar, Modeling Approaches and Computational Methods for Particle-Laden Turbulent Flows, Elsevier, Amsterdam (2023).

[29] J. Capecelatro, O. Desjardins, An Euler–Lagrange strategy for simulating particle-laden flows, *J. Comput. Phys.* 238 (2013) 1–31.

[30] S.M. Peker, S.S. Helvaci, Solid–Liquid Two Phase Flow, Elsevier, Amsterdam (2011).

[31] L. Xie, Z.H. Luo, Modeling and simulation of the influences of particle–particle interactions on dense solid–liquid suspensions in stirred vessels, *Chem. Eng. Sci.* 176 (2018) 439–453.

[32] S. Hosseini, D. Patel, F. Ein-Mozaffari, M. Mehrvar, Study of solid–liquid mixing in agitated tanks through electrical resistance tomography, *Chem. Eng. Sci.* 65 (4) (2010) 1374–1384.

[33] D. Gidaspow, Multiphase Flow and Fluidization: Continuum and Kinetic Theory Descriptions, Academic Press, Boston (1994).

[34] Z. Yang, T. Holemans, B. Lagrain, B. Sels, M. Vanierschot, A solid–liquid mixing reactor based on swirling flow technology, *Chem. Eng. Sci.* 280 (2023) 119054.

[35] F. Maluta, A. Paglianti, G. Montante, RANS-based predictions of dense solid–liquid suspensions in turbulent stirred tanks, *Chem. Eng. Res. Des.* 147 (2019) 470–482.

[36] P.R. Spalart, Strategies for turbulence modelling and simulations, *Int. J. Heat Fluid Flow* 21 (3) (2000) 252–263.

[37] L.T. Zhu, X.Z. Chen, B. Ouyang, W.C. Yan, H. Lei, Z. Chen, Z.H. Luo, Review of machine learning for hydrodynamics, transport, and reactions in multiphase flows and reactors, *Ind. Eng. Chem. Res.* 61 (28) (2022) 9901–9949.

[38] D.Y. Gu, C.S. Li, X.L. Gu, J. Wang, Solid–liquid mixing characteristics in a fractal cut impeller stirred reactor with dense solid loading, *Chem. Eng. Process. Process Intensif.* 196 (2024) 109655.

[39] Z. Yang, T. Holemans, B. Lagrain, B. Sels, M. Vanierschot, A draft tube to improve mixing in swirling flow-based solid–liquid mixing reactors, *Chem. Eng. Res. Des.* 206 (2024) 226–241.

[40] Z.L. Xu, C. Yang, L.X. Wan, B.Q. Liu, Numerical investigation on the intensification of coaxial slurry mixing systems, *Chem. Eng. Process. Process Intensif.* 192 (2023) 109514.

[41] T. Meng, A. Paglianti, F. Alberini, G. Montante, Y. Wang, Z.H. Liu, Investigating coupling and intensification mechanisms in multi-shaft digesting stirring reactors using POD, *AIChE J. (2025) e70028.*

[42] A. de Lamotte, A. Delafosse, S. Calvo, D. Toye, Identifying dominant spatial and time characteristics of flow dynamics within free-surface baffled stirred-tanks from CFD simulations, *Chem. Eng. Sci.* 192 (2018) 128–142.

[43] S.C. Zhao, W. Li, J.L. Zhang, Investigation of the temporal and spatial flow features within the high-shear mixer by modal decomposition techniques, *AIChE J.* 69 (3) (2023) e17967.

[44] J. Jin, Y. Fan, PIV experimental study on flow structure and dynamics of square stirred tank using modal decomposition, *Kor. J. Chem. Eng.* 37 (5) (2020) 755–765.

[45] W.H. Weheliye, N. Cagney, G. Rodriguez, M. Micheletti, A. Ducci, Mode decomposition and Lagrangian structures of the flow dynamics in orbitally shaken bioreactors, *Phys. Fluids* 30 (3) (2018) 033603.

[46] ANSYS Inc, ANSYS FLUENT Theory Guide Inc. Release 19.2, ANSYS Academic, Research (2019).

[47] J.M. Ding, D. Gidaspow, A bubbling fluidization model using kinetic theory of granular flow, *AIChE J.* 36 (4) (1990) 523–538.

[48] A.D. Burns, T. Frank, I. Hamill, J.M. Shi, The Favre averaged drag model for turbulent dispersion in Eulerian multi-phase flows, In: 5th International Conference on Multiphase Flow, Yokohama, Japan (2004).

[49] A. de Lamotte, A. Delafosse, S. Calvo, D. Toye, Analysis of PIV measurements using modal decomposition techniques, POD and DMD, to study flow structures and their dynamics within a stirred-tank reactor, *Chem. Eng. Sci.* 178 (2018) 348–366.

[50] X.M. de Wit, M. Fruchart, T. Khain, F. Toschi, V. Vitelli, Pattern formation by turbulent cascades, *Nature* 627 (8004) (2024) 515–521.

[51] T. Savage, N. Basha, J. McDonough, J. Krassowski, O. Matar, E.A. del Rio Chanona, Machine learning-assisted discovery of flow reactor designs, *Nat. Chem. Eng.* 1 (8) (2024) 522–531.

[52] D. Zhang, B. Ouyang, Z.H. Luo, Reaction process optimization based on interpretable machine learning and metaheuristic optimization algorithms, *Chin. J. Chem. Eng.* 84 (2025) 77–85.